



Cite this: *Phys. Chem. Chem. Phys.*, 2024, 26, 278

## Effects of surface chemistry on the mechanochemical decomposition of tricresyl phosphate†

Egheosa Ogbomo, \*<sup>abc</sup> Fakhrul H. Bhuiyan, <sup>d</sup> Carlos Ayestarán Latorre, <sup>abc</sup> Ashlie Martini <sup>d</sup> and James P. Ewen \*<sup>abc</sup>

The growth of protective tribofilms from lubricant antiwear additives on rubbing surfaces is initiated by mechanochemically promoted dissociation reactions. These processes are not well understood at the molecular scale for many important additives, such as tricresyl phosphate (TCP). One aspect that needs further clarification is the extent to which the surface properties affect the mechanochemical decomposition. Here, we use nonequilibrium molecular dynamics (NEMD) simulations with a reactive force field (ReaxFF) to study the decomposition of TCP molecules confined and pressurised between sliding ferrous surfaces at a range of temperatures. We compare the decomposition of TCP on native iron, iron carbide, and iron oxide surfaces. We show that the decomposition rate of TCP molecules on all the surfaces increases exponentially with temperature and shear stress, implying that this is a stress-augmented thermally activated (SATA) process. The presence of base oil molecules in the NEMD simulations decreases the shear stress, which in turn reduces the rate constant for TCP decomposition. The decomposition is much faster on iron surfaces than iron carbide, and particularly iron oxide. The activation energy, activation volume, and pre-exponential factor from the Bell model are similar on iron and iron carbide surfaces, but significantly differ for iron oxide surfaces. These findings provide new insights into the mechanochemical decomposition of TCP and have important implications for the design of novel lubricant additives for use in high-temperature and high-pressure environments.

Received 1st November 2023,  
Accepted 28th November 2023

DOI: 10.1039/d3cp05320b

rsc.li/pccp

### 1 Introduction

Mechanochemistry describes a wide range of phenomena where mechanical force influences chemical reactivity.<sup>1</sup> This includes reactions in ball mills, where energy is transferred from moving balls to the reactants during collisions of the balls with each other and the jar walls.<sup>2</sup> Mechanochemical reactions can be performed without solvents or heating, which can provide considerable environmental benefits over conventional routes.<sup>3</sup> The choice of ball and jar materials are known to affect reactivity for a range of processes, such as cocrystallisation<sup>4</sup>

and cycloaddition,<sup>5</sup> emphasizing the important role of the solid material. In some cases, the milling balls themselves are the catalyst of the reaction, which is known as direct mechano-catalysis.<sup>6</sup> Another example and particularly high-value application of mechanochemistry is lubricant additives that reduce wear in tribological contacts.<sup>7</sup> The most popular antiwear additive for automotive lubricants, zinc dialkyldithiophosphate (ZDDP), forms protective tribofilms on rubbing surfaces through mechanochemical processes.<sup>8–10</sup>

The tribofilm growth of ZDDP is strongly dependent on the nature of the rubbing surfaces.<sup>11</sup> Surfaces with a high elastic modulus, such as tungsten carbide,<sup>9</sup> require lower loads to form tribofilms than steel,<sup>10</sup> due to higher contact stresses. In experiments using aluminium–silicon alloys, thicker ZDDP tribofilms form on the silicon phase than the aluminium matrix, which is also due to the higher elastic modulus and thus stress.<sup>12</sup> As well as the mechanical properties of the rubbing surfaces, the surface energy can also affect ZDDP adsorption and tribofilm growth.<sup>13</sup> ZDDP forms thicker tribofilms on surfaces to which it readily adsorbs, such as steel, silicon nitride, and tungsten carbide surfaces than those where minimal adsorption occurs, such as diamond-like carbon (DLC)

<sup>a</sup> Department of Mechanical Engineering, Imperial College London, South Kensington Campus, SW7 2AZ, London, UK. E-mail: e.ogbomo21@imperial.ac.uk, j.ewen@imperial.ac.uk

<sup>b</sup> Institute of Molecular Science and Engineering, Imperial College London, South Kensington Campus, SW7 2AZ, London, UK

<sup>c</sup> The Thomas Young Centre, Imperial College London, South Kensington Campus, SW7 2AZ, London, UK

<sup>d</sup> Department of Mechanical Engineering, University of California-Merced, 5200 N. Lake Road, Merced 95343, CA, USA

† Electronic supplementary information (ESI) available. See DOI: <https://doi.org/10.1039/d3cp05320b>



and silicon carbide.<sup>14</sup> Ion-implanting alloying elements into steel can affect ZDDP tribofilm growth, nickel promotes tribofilm formation, molybdenum and chromium slows growth, while vanadium and tungsten have no significant effect.<sup>15</sup> ZDDP forms thicker tribofilms on aluminium–magnesium alloys than on either of the pure metals due to the stronger adsorption of the ZDDP molecules on the alloy.<sup>16</sup> A recent study revealed how the interplay of mechanical and chemical factors determine the tribological behaviour of ZDDP on DLC, with hydrogen-free coatings of moderate elastic modulus being most wear-resistant, while still allowing ultralow friction.<sup>17</sup> Surface chemistry can also affect other mechanochemical processes inside rubbing contacts. For example, the rate of  $\alpha$ -pinene tribopolymerisation is higher on palladium, copper oxide, nickel oxide, and chromium oxide than gold, silicon oxide, aluminium oxide, and DLC surfaces.<sup>18</sup> Moreover, the  $\alpha$ -pinene tribopolymerisation rate is higher on bare silica surfaces than hydroxylated silica.<sup>19</sup> These observations can be explained by the fact that mechanochemical processes are accelerated when the confined molecules chemisorb to one<sup>20</sup> or both<sup>21</sup> sliding surfaces, since the shear stress applied through the sliding surfaces results in more strain within the strongly adsorbed molecules.

Phosphate ester lubricant additives have numerous industrial applications due to their stability, particularly in the presence of oxygen.<sup>22</sup> Their versatility in structure including the ability to incorporate a variety of substituent groups has led to their application as lubricant additives to improve the anti-wear, boundary lubrication, antioxidant, anti-corrosion, anti-foaming, and metal deactivation performance.<sup>23</sup> Phosphate esters come in various forms, including aromatic, alkyl, thiophosphates, and metal-containing esters, and are readily accessible for commercial use.<sup>23</sup> One of the most popular of these additives is tricresyl phosphate (TCP), which has been widely employed in aviation lubricants for gas turbine engines for several decades.<sup>24</sup> The molecular structure of TCP is shown in Fig. 1. Like ZDDP, TCP is an effective antiwear additive for steel contacts.<sup>25,26</sup> An additional benefit of TCP for aviation lubricants is that the tribofilms it forms on metal surfaces slow the degradation of synthetic neopentyl polyol ester base stocks.<sup>27</sup>

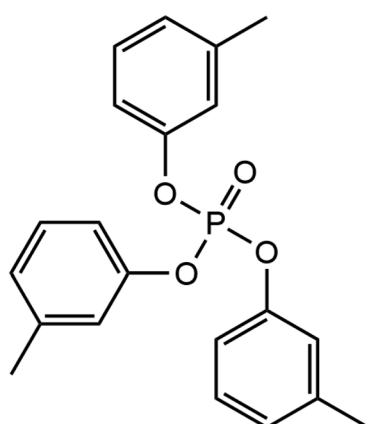


Fig. 1 Molecular structure of tri-metacresyl phosphate.

It was initially suggested that the ability of TCP to reduce wear on steel surfaces originated from polishing of the surfaces through the formation of iron phosphide.<sup>24</sup> However, later studies have shown that the major component of the tribofilms formed from TCP on steel was iron phosphate, which acted as a protective layer, rather than polishing the surfaces.<sup>28–30</sup> It has also been shown that either organic polyphosphates<sup>31</sup> or iron polyphosphates<sup>32,33</sup> are eventually formed from TCP inside tribological contacts, which are ultimately responsible for its antiwear performance on steel surfaces. At high temperatures, TCP molecules form relatively thick (60–100 nm) thermal films on steel surfaces,<sup>34</sup> however, it forms thinner tribofilms ( $\sim 20$  nm) on rubbing surfaces.<sup>26</sup> This is much thinner than the ZDDP tribofilms that form on rubbing steel surfaces ( $\sim 100$  nm).<sup>26</sup>

The thermal decomposition of TCP has been studied on several different substrates. Wheeler and Faut<sup>35</sup> used X-ray photoelectron spectroscopy (XPS) to compare the adsorption and dissociation of TCP on gold and iron surfaces. On both substrates, adsorption saturated at about one monolayer, but adsorption was slower on gold than on iron.<sup>35</sup> TCP underwent non-dissociative adsorption on gold and desorbed upon heating, with no TCP left on the surface at 473 K.<sup>35</sup> On iron, no desorption occurred upon heating and additional interactions were observed between the substrate and the tolyl groups on the TCP molecule.<sup>35</sup> TCP decomposed on iron between 423 K and 473 K with one of the tolyl groups being removed to form iron phosphate.<sup>35</sup> The temperature range for decomposition is close to the temperature at which TCP significantly reduced the friction of rubbing steel surfaces in tribometer experiments.<sup>30</sup> It has since been shown that the thermal decomposition of TCP on iron surfaces occurs mainly *via* P–O bond scission to form methylphenoxy intermediates.<sup>36</sup> When TCP was heated to 800 K on iron, the methylphenoxy intermediates either desorbed as cresol *via* hydrogenation or decomposed further to generate tolyl intermediates.<sup>36</sup> Some of these tolyl intermediates desorbed as toluene *via* hydrogenation, but the majority decomposed resulting in hydrogen and carbon monoxide desorption and carbon deposition onto the iron surface.<sup>36</sup>

The steel surfaces inside tribological contacts are chemically heterogeneous and are covered by multiple different iron oxides.<sup>37,38</sup> From experiments conducted at high temperature (750 K), it was suggested that, due to acid–base reactions, TCP vapor preferentially reacts with iron in higher oxidation states, with reactivity increasing in the order:  $\text{Fe} < \text{FeO} < \text{Fe}_3\text{O}_4 < \text{Fe}_2\text{O}_3$ .<sup>32</sup> However, more recent experiments suggested that reactivity towards TCP increases in the order  $\text{Fe}_3\text{O}_4 < \text{Fe} < \text{Fe}_2\text{O}_3$ .<sup>39</sup> In both of these experimental studies, the iron surfaces will also form oxide layers that react with the TCP, rather than the native metal.<sup>39</sup> In addition to surface oxides, metal carbides are another important component of bearing steels.<sup>40</sup> A previous study of thermal decomposition found that TCP reactivity increases in the order: tungsten carbide  $<$  molybdenum carbide  $<$  chromium carbide  $<$  vanadium carbide.<sup>41</sup>

In recent years, experimental studies of TCP adsorption and decomposition have been complemented by molecular simulations. For example, Khajeh *et al.*<sup>42</sup> used molecular dynamics

(MD) simulations with a reactive force field (ReaxFF) to study the adsorption of TCP on hydroxylated amorphous  $\text{Fe}_3\text{O}_4$ . They found that, at lower temperatures ( $\leq 500$  K), chemisorption occurred mostly *via* Fe-C bond formation through the tolyl groups. At higher temperatures (600–700 K), a significant amount of Fe-O and O-P bonding also occurred, indicating chemisorption through the central phosphate group. Ewen *et al.*<sup>44</sup> compared the chemisorption and dissociation of TCP to trialkyl phosphates on  $\text{Fe}_3\text{O}_4(001)$  surfaces. In agreement with previous experiments,<sup>36,45</sup> they found that the triaryl phosphate TCP was much less reactive compared to the trialkyl phosphates. The MD simulations also showed that, while the main decomposition mechanism for trialkyl phosphates was C-O bond dissociation, the only bonds that broke in TCP were P-O bonds.<sup>44</sup> For the trialkyl phosphates, Ewen *et al.*<sup>44</sup> also compared the adsorption and dissociation on  $\text{Fe}_3\text{O}_4(001)$  to hydroxylated amorphous  $\text{Fe}_3\text{O}_4$  and  $\alpha$ -Fe surfaces. They found that the reactivity of the trialkyl phosphates increased in the order: hydroxylated amorphous  $\text{Fe}_3\text{O}_4$  <  $\text{Fe}_3\text{O}_4(001)$  <  $\alpha$ -Fe. Ayestarán Latorre *et al.*<sup>46</sup> studied the mechanochemical decomposition of trialkyl phosphates between sliding iron surfaces using non-equilibrium molecular dynamics (NEMD) simulations with ReaxFF. They found that secondary trialkyl phosphates were much more reactive than primary ones,<sup>46</sup> in agreement with previous experiments on ZDDP.<sup>10</sup> The influence of surface chemistry on the mechanochemical response of organophosphates is yet to be explored either experimentally or through NEMD simulations.

In this study, we use NEMD simulations with ReaxFF to compare the mechanochemical decomposition of TCP molecules confined between different ferrous surfaces over a range of temperatures and pressures. We observe significant differences in the mechanochemical reactivity of TCP on iron, iron oxide, and iron carbide surfaces. The variations in reactivity can be explained by differences in surface energy and stiffness, which can be accounted for in theoretical models for mechanochemistry.

## 2 Methodology

### 2.1 System setup

We used NEMD simulations<sup>47</sup> to compare the mechanochemical reactivity of TCP on three ferrous surfaces, as shown in Fig. 2. This is a molecule composed of three cresyl (methylphenyl) groups linked to a phosphate group. TCP is produced from cresol, which naturally contains a mixture of isomers with the methyl group in the *ortho*-, *meta*- and *para*-positions. The *ortho*-isomers of TCP are known to be toxic and modern production methods have reduced the concentration of these to very low levels.<sup>48</sup> Therefore, the TCPs used in current aviation lubricants generally contain mixtures of the *meta*-isomers and also some *para*-isomers.<sup>48</sup> The *para*-isomers were shown to have poorer lubricating properties compared to mixtures of isomers.<sup>29</sup> However, a recent study showed that the *para*-isomer is only slightly more reactive than the *meta*-isomer on ferrous surfaces.<sup>39</sup> In this study, we chose to

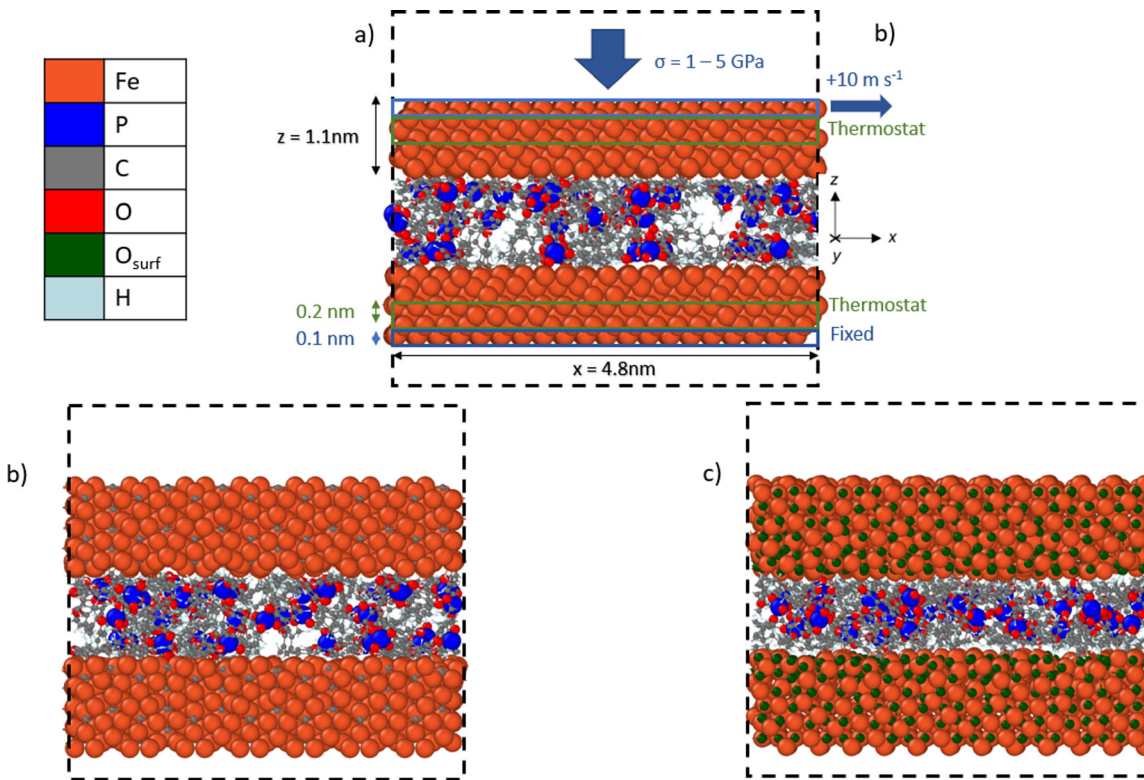


Fig. 2 Side-view snapshots showing the model systems with TCP molecules confined between (a)  $\alpha$ -Fe(110), (b)  $\text{Fe}_3\text{C}(010)$ , and (c)  $\text{Fe}_3\text{O}_4(001)$ -SCV surfaces. Systems shown after minimisation and equilibration, but before heating, compression, and shear. Black dashed line shows the simulation box. Rendered using OVITO.<sup>42</sup>



study pure tri-meta-cresyl phosphate for simplicity; its molecular structure is shown in Fig. 1.

All the systems were constructed using the materials and processes simulations (MAPS) platform from Scienomics SARL. The three model surfaces were native iron, cementite, and magnetite. Symmetrical contacts were used with the same material for the upper and lower surface. Native iron surfaces were considered due to the possibility that they are exposed to the additive following removal of surface oxides in rubbing steel contacts.<sup>49</sup> Cementite was chosen as a representative iron carbide surface because it was identified in previous thermal degradation experiments using TCP.<sup>50</sup> Magnetite was selected since previous experiments have shown that it is the major oxide formed on the surface of bearing steel following tribometer experiments.<sup>37</sup> We used an  $\alpha$ -Fe(110) for the iron surface,<sup>51</sup> Fe<sub>3</sub>C(010) as the cementite surface,<sup>52</sup> and Fe<sub>3</sub>O<sub>4</sub>(001) with a subsurface cation vacancy (SCV) reconstruction as the magnetite surface<sup>53</sup> due to their relatively low surface energies.

Periodic boundary conditions were applied in the  $x$  and  $y$  directions. Since the materials all had different lattice constants, it was not possible to create periodic surfaces with exactly the same dimensions. The  $\alpha$ -Fe(110) surfaces had dimensions of  $x = 4.8$ ,  $y = 4.8$  and  $z = 1.1$  nm. The Fe<sub>3</sub>C(010) surfaces had dimensions of  $x = 4.9$ ,  $y = 4.7$  and  $z = 1.05$  nm. The Fe<sub>3</sub>O<sub>4</sub>(001) surfaces had dimensions of  $x = 5.0$ ,  $y = 5.0$  and  $z = 1.1$  nm. At the start of the simulations, two of each type of surface were separated by a 3.0 nm in the  $z$ -direction. A fixed boundary condition is applied in the  $z$ -direction.

To replicate tribometer experiments under full-film EHL conditions,<sup>9,10,54</sup> we ensured that no direct contact between the sliding ferrous surfaces occurred during the simulations. In most of the NEMD simulations, 48 TCP molecules were randomly inserted between the surfaces, leading to a fluid film thickness of approximately 1 nm. Experiments have shown that the molecular area of TCP is around 1.1 nm<sup>2</sup> at the air–water interface.<sup>55</sup> The molecular area of TCP on ferrous surfaces is likely to be similar as on the air–water interface, as shown for other surfactants.<sup>56</sup> Thus, the chosen number of molecules is representative of the surface coverage expected for one TCP monolayer adsorbed on each of the two confining surfaces (24 molecules/~25 nm<sup>2</sup>). Previous experiments have confirmed that monolayers of TCP adsorb on ferrous surfaces both from the vapour phase<sup>35,57</sup> and also from toluene solution.<sup>28</sup>

While the main application of TCP is as an additive dissolved in a base oil for aviation lubricants,<sup>22</sup> it can also be used as a lubricant as a pure substance in both the liquid phase<sup>30</sup> and the vapour phase for high-temperature applications.<sup>58</sup> Due to the significant additional computational expense of simulating non-reactive base oil molecules, these were excluded from the majority of our simulations. Although some reactive NEMD simulation studies of lubricant additive mechanochemistry have simulated the base oil molecules,<sup>59,60</sup> the vast majority have not.<sup>21,46,61–63</sup> Previous NEMD simulations of sulfur-based additives with ReaxFF have shown that there were only minor differences when unreactive base oils were included in the simulations.<sup>59</sup> To assess the effect of including base oil molecules

in our systems, we performed a subset of simulations that contained 48 TCP molecules randomly mixed with 48 diisodecyl adipate molecules (DIDA)<sup>34</sup> between  $\alpha$ -Fe(110) surfaces. This is the same molar ratio used in a previous NEMD simulations of additive-base oil systems.<sup>59</sup> Although the concentration of TCP used in commercial formulations (1–5%)<sup>64</sup> and tribometer experiments ( $\leq 10\%$ )<sup>65</sup> is typically much lower than 50%, this represents a reasonable compromise between computational efficiency and closeness to real-life applications.

## 2.2 Simulation details

All the simulations were performed using the large-scale atomic/molecular massively parallel simulator (LAMMPS) open-source software.<sup>66</sup> The velocity Verlet<sup>67</sup> integration scheme was used with a timestep of 0.25 fs.<sup>43</sup> The simulations were conducted in three phases: energy minimisation, equilibration, and then simultaneous heating, compression, and shear. The energy minimisation phase was conducted using the conjugate gradient method. For all the systems and conditions investigated, equilibration was performed at an ambient temperature of 300 K for 0.1 ns. During the equilibration phase, the two ferrous surfaces were brought closer together by applying a low pressure of 10 MPa. The system was pressurised by applying a constant normal force ( $z$ -direction) equally distributed across the topmost layer of atoms (0.1 nm) in the upper surface, as shown in Fig. 2a. The lowermost layer of atoms (0.1 nm) in the bottom surface was kept fixed in the  $z$ -direction. The equilibration at 10 MPa ensured that a realistic liquid density of TCP ( $1.2 \pm 0.1$  g cm<sup>-3</sup>) was obtained prior to the heating, compression, and shear phase.

Following the equilibration phase, the compression and shear phase of the simulations were run for 1 ns. Here, a constant sliding velocity of 10 m s<sup>-1</sup> was applied to the outer layer of atoms in the upper surface in the  $x$ -direction, as shown in Fig. 2a. This is representative of the sliding velocities found in lubricated components inside gas turbine engines and tribometer experiments with TCP, which have been performed at sliding velocities as high as 10 m s<sup>-1</sup>.<sup>64</sup> The pressure was increased to the target value of 1–5 GPa using the same method as during the equilibration. The temperatures were increased to 400–900 K using a Langevin thermostat with a damping parameter of 25 fs.<sup>68</sup> The thermostat acted only in the  $y$ -direction and on the central layer of atoms (0.2 nm) in the upper and lower surfaces, as shown in Fig. 2a. This approach enabled a temperature gradient to develop in the centre of the TCP film and heat to be dissipated at the surfaces, as would occur experimentally.<sup>69</sup> The thermostat was sufficiently efficient to ensure that the average system temperature was within 10 K of the target value at the chosen sliding velocity. The selected range of temperatures and pressures spans those expected in applications of TCP such as antiwear additives in gearboxes for gas turbine engines<sup>26</sup> and as vapour-phase lubricants.<sup>58</sup>

The temperature, pressure, and sliding velocity were all increased simultaneously to capture their combined effects on the reaction rate. Some previous NEMD simulations of mechanochemical reactions with ReaxFF have isolated the effects of temperature, pressure, and sliding by using separate



phases of the simulations.<sup>20,62,70</sup> The number of additive molecules in the NEMD simulations is finite, so separating the simulations into different phases (thermalisation, pressurisation, and sliding) means that fewer molecules are available to react in any subsequent phases. Conversely, in experimental mechanochemistry studies,<sup>9,10,54</sup> additive-containing lubricants are entrained between the sliding surfaces, continuously replenishing the number of additive molecules. Hence, in our NEMD simulations, we elected to increase the temperature, pressure, and sliding velocity to their target values concurrently.<sup>46</sup>

**2.2.1 Force field details and validation.** We used the bond order-based ReaxFF potential for all of the NEMD simulations. Similar systems consisting of phosphorus-containing additives confined between iron surfaces have previously been studied with NEMD simulations using first principles methods.<sup>61,71</sup> However, bond order potentials are several orders of magnitude cheaper than first principles methods,<sup>72</sup> allowing much larger systems to be simulated under experimentally-relevant conditions. ReaxFF was originally developed by van Duin *et al.*<sup>73</sup> to study hydrocarbon reactivity and has been parameterised to model a wide range of chemical systems and processes.<sup>74</sup> Of particular relevance to this study, ReaxFF-based NEMD simulations are now routinely used to study tribochemical reactions.<sup>75</sup> The C/H/O/Fe/P ReaxFF parameters used in this study were developed by Khajeh *et al.*<sup>43</sup> The parameters for Fe/O/H were originally developed by Aryanpour *et al.*,<sup>76</sup> Fe/C by Zou *et al.*,<sup>77</sup> P/O/C/H by Verlackt *et al.*,<sup>78</sup> and C/H/O by Chenoweth *et al.*<sup>79</sup> The point charges on the atoms vary dynamically during the simulations and were calculated using the charge equilibration (QEeq) method.<sup>80</sup> Chemical bonding information was output every 1.0 ps, using a bond order cutoff of 0.3 to identify covalent bonds.<sup>43</sup> The choice of bond order cutoff only affects the post-processing analysis and does not influence the ReaxFF energy or force calculations during then NEMD simulations.

The combined C/H/O/Fe/P ReaxFF parameters<sup>43</sup> have been successfully applied to study the thermal and mechanochemical decomposition of phosphate esters with different alkyl and aryl substituents on several ferrous surfaces.<sup>39,44,46</sup> The ReaxFF parameters have also been validated against first principles calculations for the non-dissociative adsorption energy, C–O bond dissociation energy, and P–O bond dissociation energy for trialkyl phosphates on  $\alpha$ -Fe(110).<sup>44</sup> The ReaxFF parameters for Fe/O/H have been shown to accurately reproduce the experimental lattice constants for  $\alpha$ -Fe (within 1%),<sup>77</sup> Fe<sub>3</sub>C (within 0.5%),<sup>77</sup> and Fe<sub>3</sub>O<sub>4</sub> (within 3%).<sup>76</sup> The ReaxFF parameters have also been shown to perform favourably compared to other many-body force fields in describing the mechanical properties of  $\alpha$ -Fe.<sup>81</sup> At 300 K, the experimental elastic modulus is 166 GPa for  $\alpha$ -Fe,<sup>82</sup> 174 GPa for Fe<sub>3</sub>C,<sup>83</sup> and 186 GPa for Fe<sub>3</sub>O<sub>4</sub>(100).<sup>84</sup> With the ReaxFF parameters used here,<sup>43,76,77</sup> the bulk elastic modulus at 300 K is 136 GPa for  $\alpha$ -Fe,<sup>85</sup> 148 GPa for Fe<sub>3</sub>C,<sup>85</sup> and 129 GPa for Fe<sub>3</sub>O<sub>4</sub>.<sup>86</sup> Thus, at 300 K, the experimental bulk elastic modulus is underpredicted by 18% for  $\alpha$ -Fe, 15% for Fe<sub>3</sub>C, and 31% for Fe<sub>3</sub>O<sub>4</sub>. Since previous density functional theory (DFT) calculations have highlighted the

importance of contact stiffness to mechanochemical processes,<sup>87</sup> we also calculated the elastic properties of thin single slabs of the three materials used in the NEMD simulations. For this calculation, the lowermost layer of atoms in each slab of material was fixed in the *z*-direction, while a constant normal force was applied the topmost layer of atoms to compress the system to 2 GPa. The temperature was varied between 300–900 K using the same thermostat as applied in the NEMD simulations. The corresponding elastic constant ( $C_{33}$ ) was calculated from the strain fluctuations at constant normal stress.<sup>88</sup> The elastic constant results for the thin slabs are shown in the ESI† (Table S1). For the  $\alpha$ -Fe(110) slabs, the elastic constant  $C_{33}$  decreases from 206 GPa at 300 K to 196 GPa at 900 K. The elastic constant  $C_{33}$  also decreases with increasing temperature for the Fe<sub>3</sub>C(010) (from 200 GPa to 181 GPa) and Fe<sub>3</sub>O<sub>4</sub>(001) (from 220 GPa to 196 GPa) slabs. The higher stiffness of thin solid slabs compared to bulk solids was also observed in previous MD simulations and was attributed to geometrical confinement.<sup>89</sup> The decreasing stiffness with increasing temperature is also consistent with previous experiments.<sup>82</sup>

## 3 Results and discussion

### 3.1 Base oil effects on TCP decomposition

The primary application of TCP is as an antiwear additive for aviation lubricants where it is dissolved in a base oil.<sup>22</sup> Thus, to ensure that not simulating the base oil molecules did not significantly affect the mechanochemical decomposition mechanism, we performed a subset of simulations containing 50% TCP and 50% DIDA molecules. Despite some bonding of DIDA molecules to the surfaces, negligible decomposition of the ester base oil occurs during the simulations (<2 molecules). Previous experiments have suggested that ester base oil decomposition may become significant when it is heated for several hours with a stainless steel coupon at temperatures above about 600 K.<sup>65</sup> However, this process is much slower than TCP decomposition, which occurred experimentally at much lower temperatures.<sup>65</sup> The mechanochemical decomposition mechanism of TCP is also unaffected by the presence of base oil molecules. This observation is consistent with previous NEMD simulations, which showed that the addition of dodecane base oil molecules did not affect the mechanochemical reaction pathway of sulfur-based lubricant additives on ferrous surfaces.<sup>59</sup>

For a given normal stress, the shear stress is much lower for the 50% TCP, 50% DIDA system than the 100% TCP system, as shown in the ESI† (Fig. S1). This reduction in shear stress is expected to due the lubricating effect of the low-friction ester base oil.<sup>90</sup> From previous mechanochemistry experiments of ZDDP tribofilm growth,<sup>9,10,91</sup> it is anticipated that the lower shear stress will result in lower reactivity for the 50% TCP, 50% DIDA than the 100% TCP system.

Fig. 3a shows the change in the number of intact TCP molecules for 100% TCP at 600 K and 1–5 GPa, while Fig. 3b



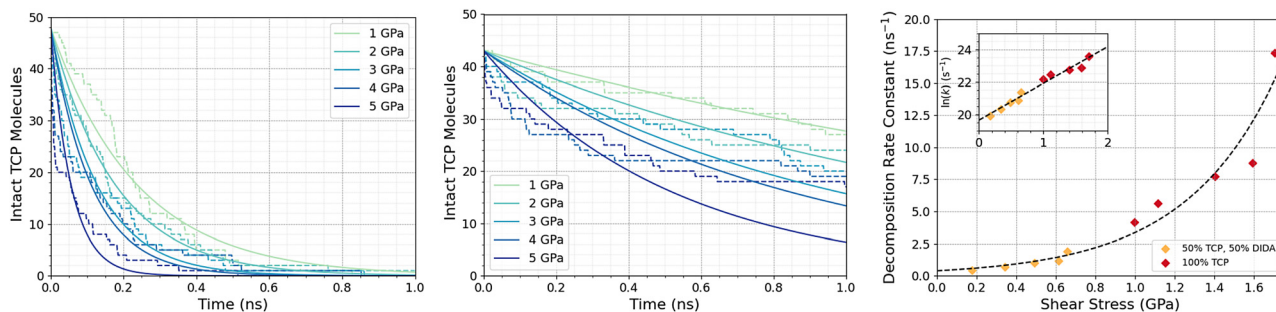


Fig. 3 Change in the number of intact TCP molecules with time at 600 K and 1–5 GPa for (a) 100% TCP system (b) 50% TCP, 50% DIDA system. The dashed lines show the simulation data and the solid lines are exponential decay fits used to calculate the first-order rate constants,  $k$ . (c) Change in  $k$  for TCP decomposition with shear stress,  $\tau$ . The data with and without DIDA can be fit using eqn (1) with a single activation volume ( $13.6 \pm 2.6 \text{ \AA}^3$ ). Inset shows the same data versus  $\ln(k)$ .

shows the same for the 50% TCP, 50% DIDA system. The TCP molecules are counted as dissociated, *i.e.*, no longer intact, if any bond other than a C–H is broken. The number of TCP molecules decreases faster for the pure TCP system than the 50% TCP, 50% DIDA system. For both systems, there is an exponential decay of the number of intact TCP molecules with time, which is indicative of a first-order reaction.<sup>92</sup> For first-order reactions, the reaction rate,  $r = k[C]$ , where  $k$  is the rate constant and  $[C]$  is the concentration of reactant. Previous NEMD simulations showed that the mechanochemical decomposition of trialkyl phosphate decomposition between  $\alpha$ -Fe(110) surfaces also followed first-order kinetics.<sup>46</sup> In mechanochemistry experiments with ZDDP, the rate of tribofilm growth followed either zero-order or fractional-order kinetics.<sup>8,10,54</sup> The observation of zero-order kinetics indicates that the rate-determining step for tribofilm growth involves surface-adsorbed molecules,<sup>10</sup> which masks the underlying first-order kinetics.<sup>93</sup> In experiments, the surface-adsorbed additive molecules are continually replenished from the base oil solution and the bulk concentration does not significantly decrease.<sup>10</sup> On the other hand, there is a finite number of additive molecules in the NEMD simulations, which means that the decomposition rate inevitably decreases with time as fewer molecules become available to react.<sup>46</sup>

Fig. 3c shows the change in the decomposition rate constants,  $k$ , with shear stress for the 100% TCP and 50% TCP, 50% DIDA systems. The  $k$  values were determined from the exponential decay fits shown in Fig. 3a and b and the shear stress values were taken from Fig. S1 (ESI<sup>†</sup>). For all the systems and conditions shown in Fig. 3,  $k$  increases exponentially with shear stress, suggesting that TCP decomposition is a stress-augmented thermally activated (SATA) processes.<sup>94</sup> The Bell model<sup>95</sup> can be used to describe the kinetics of SATA processes:

$$k = A \exp\left(-\frac{E_a - \tau\Delta V^*}{k_B T}\right) \quad (1)$$

where  $A$  is the pre-exponential factor,  $E_a$  is the activation energy,  $\Delta V^*$  is the activation volume, and  $k_B$  is the Boltzmann constant.  $\Delta V^*$  is sometimes interpreted as volume change that occurs when the transition state is formed from the reactants.<sup>96</sup> In our simulations, as well as previous experiments of ZDDP tribofilm growth,<sup>8,10,54</sup>  $\Delta V^*$  is positive, indicating that the

volume of the transition state is larger than the reactants, confirming that the rate-determining step involves bond breaking.<sup>91</sup> We use shear stress,  $\tau$ , in eqn (1) rather than normal stress,  $\sigma$ . Previous experiments have shown that tribofilm growth is primarily controlled by shear stress and not the normal stress.<sup>9,10,91</sup> Moreover, from Fig. 3c, it is clear that the higher shear stress in the 100% TCP system leads to larger  $k$  values than for the 50% TCP, 50% DIDA systems, even at identical normal stress (Fig. S1, ESI<sup>†</sup>). The combined rate constant *versus* shear stress data set (100% TCP and 50% TCP, 50% DIDA) can be described with a single fit to eqn (1) (dashed line in Fig. 3c), yielding an activation volume of  $13.6 \pm 2.6 \text{ \AA}^3$ . This value is within the uncertainty range of the activation volume calculated for a 100% TCP system under the same conditions ( $10.7 \pm 6.2 \text{ \AA}^3$ ). Thus, the reduction in  $k$  for the 50% TCP, 50% DIDA system compared to 100% TCP can be fully explained by the decrease in the shear stress, which is due to the lubricating effect of the low-friction DIDA molecules.<sup>9,10,91</sup> There do not seem to be any other interactions between the DIDA base oil molecules and the iron surface or TCP molecules that directly reduce the reaction rate. Therefore, due to the much lower computational expense, we simulate pure TCP systems for the remainder of this study.

### 3.2 Surface chemistry effects on shear stress

We compared the change in the shear stress with normal stress for the iron, iron carbide, and iron oxide systems, as shown in Fig. 4. The steady-state shear stress was block averaged over the final 0.5 ns of the NEMD simulations. At all the studied temperature and normal stress conditions, the shear stress is lower for the systems with TCP molecules sheared between iron oxide surfaces than iron and iron carbide surfaces. For all three surfaces, the shear stress increases linearly with normal stress with a finite intercept, as predicted by the extended Amontons–Coulomb law:  $\tau = \mu\sigma + \tau_0$ , where  $\tau$  is the shear stress,  $\mu$  is the friction coefficient,  $\tau_0$  is the Derjaguin offset, and  $\sigma$  is the normal stress.<sup>97</sup> The friction coefficient and Derjaguin offset for the different systems and temperatures are shown in the ESI<sup>†</sup> (Tables S2 and S3). The friction coefficient, given by the gradient of the linear fits in Fig. 4, is similar for all three surfaces. The Derjaguin offset, given by the intercept of the



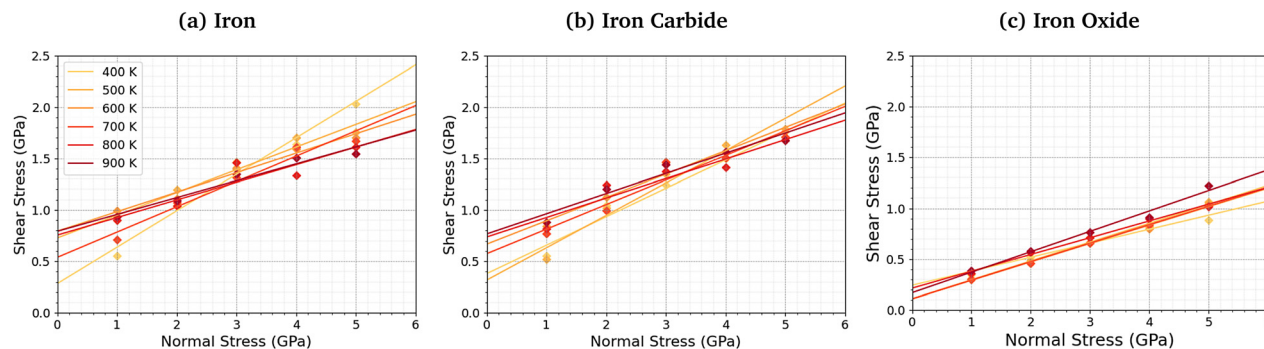


Fig. 4 Variation in shear stress with changes in normal stress for (a)  $\alpha$ -Fe(110), (b)  $\text{Fe}_3\text{C}(010)$ , and (c)  $\text{Fe}_3\text{O}_4$  (001) surfaces.

linear fit, is similar for iron and iron carbide surfaces, but is around 50% lower for iron oxide. This is likely due to the higher surface energy and adhesion of TCP molecules on iron and iron carbide compared to iron oxide.<sup>13</sup> Previous DFT calculations suggested that the surface energy of  $\alpha$ -Fe(110) ( $2.3 \text{ J m}^{-2}$ )<sup>51</sup> and  $\text{Fe}_3\text{C}(010)$  ( $2.2 \text{ J m}^{-2}$ )<sup>52</sup> is much larger than  $\text{Fe}_3\text{O}_4$ (001) ( $1.0 \text{ J m}^{-2}$ ).<sup>98</sup>

For the iron and iron carbide systems, the friction coefficient decreases with increasing temperature (Table S2, ESI†); in contrast, the Derjaguin offset increases with increasing temperature (Table S3, ESI†). As the temperature increases, the amount of TCP decomposition will also increase,<sup>44</sup> which affects the temperature-dependence of the friction coefficient and Derjaguin offset. For the iron oxide surfaces, the temperature has a negligible effect on the friction coefficient and Derjaguin offset, which is probably due to the much lower reactivity of TCP on this surface.<sup>44</sup> The addition of base oil

molecules as well as TCP molecules between the iron surfaces leads to a large reduction in the Derjaguin offset ( $\tau_0 = 0.79 \text{ GPa}$  to  $\tau_0 = 0.20 \text{ GPa}$ ), but a negligible change in the friction coefficient ( $\mu = 0.18$  to  $\mu = 0.17$ ), as shown in Fig. S1 (ESI†). This observation is in agreement with previous NEMD simulations of iron surfaces lubricated by monolayers formed from polar lubricant additive molecules.<sup>99</sup> Consequently, if lubricant molecules were added to the iron carbide and iron carbide systems, the shear stress conditions would probably be similar for all the surfaces.

### 3.3 Surface chemistry effects on TCP dissociation

Fig. 5 shows the change in the number of intact TCP molecules with time for  $\alpha$ -Fe(110),  $\text{Fe}_3\text{C}(010)$ , and  $\text{Fe}_3\text{O}_4$ (001) surfaces at constant normal stress (4 GPa) and varied temperature (400–900 K), and constant temperature (600 K) and varied normal

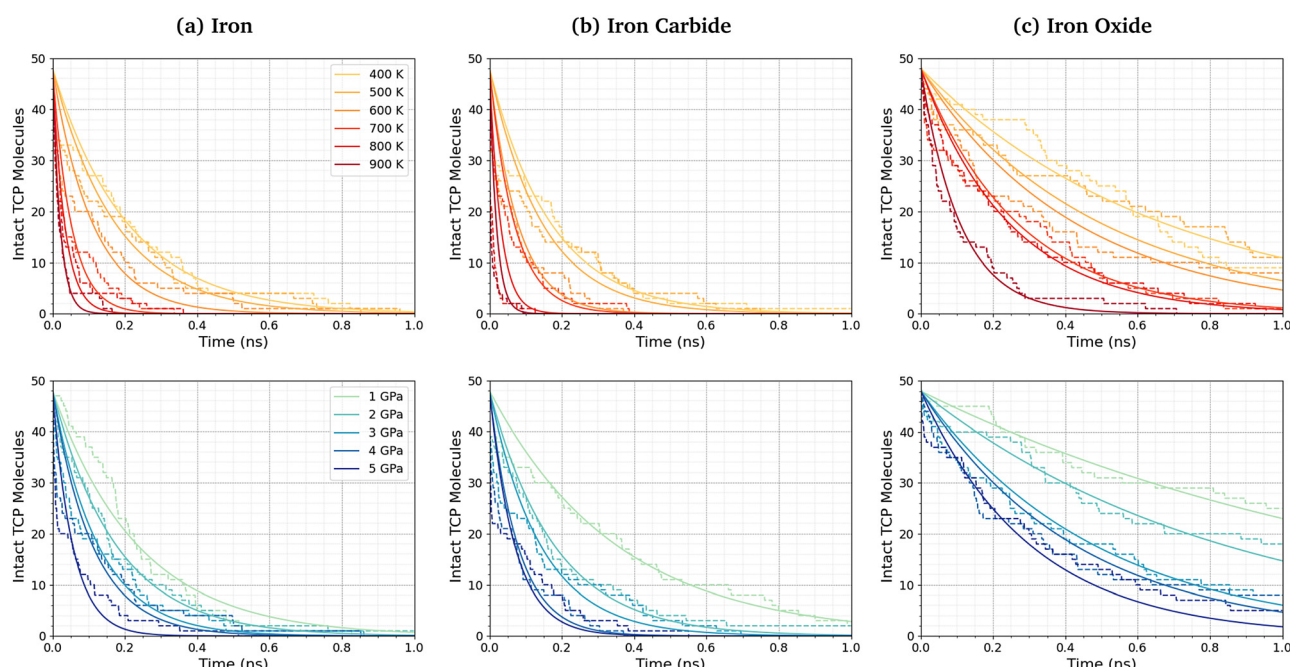


Fig. 5 Number of intact TCP molecules with time at 4 GPa between 400–900 K (top row) and at 600 K between 1–5 GPa (bottom row) for (a)  $\alpha$ -Fe(110), (b)  $\text{Fe}_3\text{C}(010)$ , and (c)  $\text{Fe}_3\text{O}_4$ (001) surfaces. The dashed lines show the simulation data and the solid lines are exponential decay fits used to calculate the first-order rate constants,  $k$ .



stress (1–5 GPa). Results for other conditions are shown in the ESI† (Fig. S2). The exponential decay curves are used to calculate the TCP decomposition rate constant,  $k$ , for each temperature and stress condition. Ayestarán Latorre *et al.*<sup>46</sup> investigated the mechanochemical decomposition of trialkyl phosphates between 300–500 K and 1–4 GPa for  $\alpha$ -Fe(110) surfaces. Comparing the current results to this previous study, it is clear that triaryl phosphates such as TCP have much lower decomposition rate constants than trialkyl phosphates under the same conditions. This observation agrees with previous experimental<sup>36,45</sup> and simulation<sup>44</sup> studies of the thermal decomposition of phosphate esters on ferrous surfaces.

The TCP decomposition rate constants,  $k$ , vary significantly depending on the surface chemistry, with the fastest reactions being observed for the  $\alpha$ -Fe(110) systems, followed by  $\text{Fe}_3\text{C}(010)$ , and finally  $\text{Fe}_3\text{O}_4(100)$ . This may be due to the differences in surface energies of the three ferrous surfaces, as discussed in the previous section.<sup>51,52,98</sup> Higher surface energies promote stronger molecular adsorption<sup>100</sup> and thus faster TCP decomposition. Indeed, DFT calculations have shown that adsorption is a crucial step the decomposition of TCP on iron surfaces.<sup>101</sup>

Previous high-temperature (750 K) thermal decomposition experiments suggested that TCP preferentially reacted with iron oxides that were in a higher oxidation state, *i.e.*  $\text{Fe} < \text{FeO} < \text{Fe}_3\text{O}_4 < \text{Fe}_2\text{O}_3$ .<sup>32</sup> This contrasts with first principles NEMD simulations of other lubricant additives, such as molybdenum dithiocarbamates, where native iron surfaces were found to be much more reactive than oxidised surfaces.<sup>63</sup> We observe much higher mechanochemical reactivity on the iron surface compared to the iron oxide surface, which is in agreement with the simulations,<sup>63</sup> but not the experiments.<sup>32</sup> This is probably because the iron used surfaces in the experiments<sup>32</sup> were also covered by an oxide layer rather than the native iron surfaces used in the simulations.<sup>39</sup>

No direct Fe–P bonds formed between the surfaces and TCP molecules in any of the NEMD simulations, but a large number of new Fe–O bonds form. This observation indicates that iron phosphate, rather than iron phosphide, is formed on the ferrous surfaces, which is consistent with observations in previous experimental studies.<sup>28–30</sup> Previous MD simulations investigating the thermal decomposition of TCP on hydroxylated

amorphous  $\text{Fe}_3\text{O}_4$  have shown that the initial step involved Fe–C bonding.<sup>43</sup> Indeed, DFT investigations have shown that benzene chemisorbs on iron oxide surfaces due to strong interactions between iron cations and the aromatic  $\pi$ -electrons.<sup>102</sup> To investigate this further, we quantified the change in the number of Fe–C bonds formed at different pressures and temperatures. The Fe–C bonds present in the  $\text{Fe}_3\text{C}(010)$  surfaces before exposure to TCP are not included in the analysis. Fig. 6 shows the variation in the number of Fe–C bonds with time for the simulated TCP systems at 600 K between 1–5 GPa for  $\alpha$ -Fe(110),  $\text{Fe}_3\text{C}(010)$ , and  $\text{Fe}_3\text{O}_4(100)$ . The number of Fe–C bonds at a given time increases as  $\text{Fe}_3\text{O}_4(100) < \text{Fe}_3\text{C}(010) < \alpha\text{-Fe}(110)$ , which is the same order observed for the rate constants of TCP decomposition on the three surfaces. We also see a clear trend of an increase in the number of Fe–C bonds, and therefore chemisorption of TCP, with an increase in pressure for all three surfaces. The increased bonding of the TCP carbon atoms on  $\alpha\text{-Fe}(110)$  compared to  $\text{Fe}_3\text{C}(010)$  and  $\text{Fe}_3\text{O}_4(100)$  can be visualised in the number density profiles shown in the ESI† (Fig. S3). The carbon peaks from the TCP molecules show increased overlap with the iron peaks for  $\alpha\text{-Fe}(110)$  compared to the other surfaces.

Fig. 7 shows the relationship between the number of Fe–C bonds formed and the TCP decomposition rate constant. There is a logarithmic increase in the TCP decomposition rate constant with the number of Fe–C bonds formed for all three surfaces. This implies that increased chemisorption of the molecules leads to faster dissociation.<sup>13</sup> Indeed, previous experiments have shown that ZDDP forms thicker tribofilms on surfaces to which it more strongly adsorbs.<sup>14</sup>

### 3.4 TCP decomposition mechanisms

Fig. 8 shows the change in the total number of C–O and P–O bonds with sliding time for an intermediate temperature (500 K) and pressure (3 GPa). For the  $\text{Fe}_3\text{O}_4$  (001) surfaces, bonds formed with surface oxygen atoms are included in the analysis. The red lines represent the total change in the number of bonds P–O bonds compared to the initial TCP molecules, the blue lines show the contribution from P–O bonds in TCP that are broken, and purple lines show new bonds that are formed. A negligible number of new C–O bonds form in the simulations and the total change is shown by the solid green lines. For all the surfaces, P–O cleavage precedes C–O cleavage and, by the

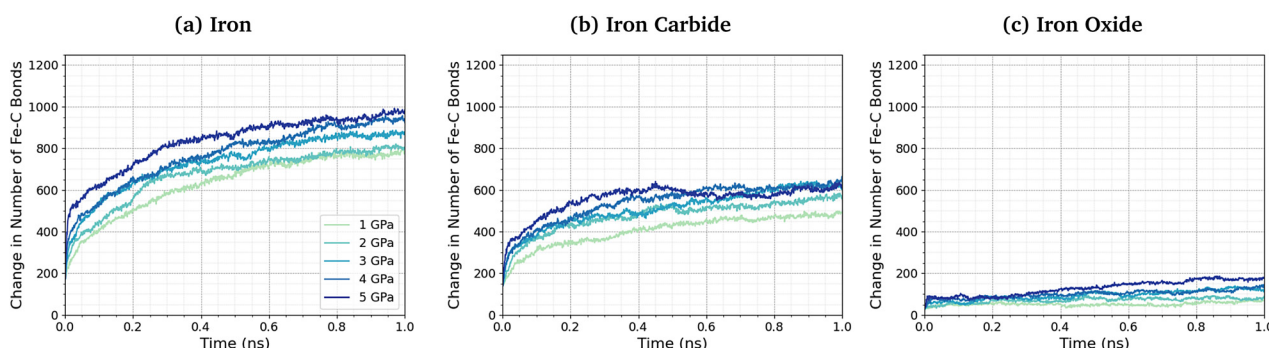


Fig. 6 Change in the number of Fe–C bonds with simulation time at 600 K between 1–5 GPa for (a)  $\alpha\text{-Fe}(110)$ , (b)  $\text{Fe}_3\text{C}(010)$ , and (c)  $\text{Fe}_3\text{O}_4(100)$ .



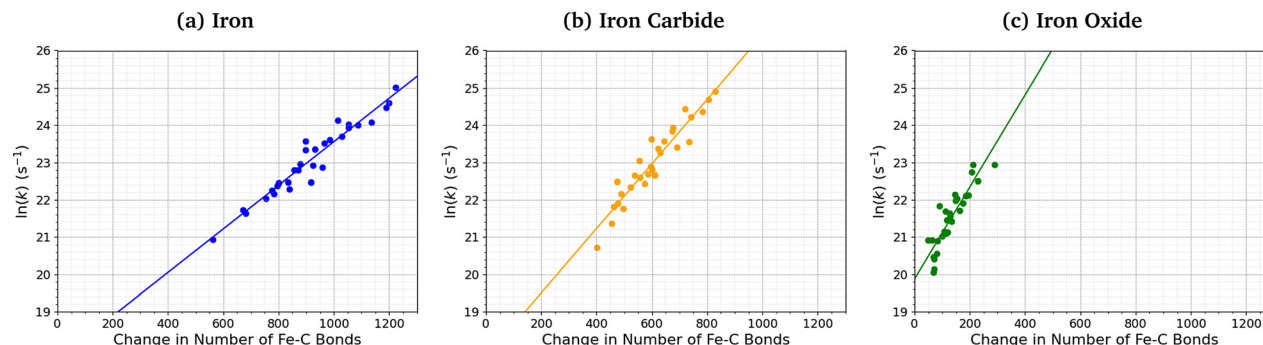


Fig. 7 Variation in  $\ln(k)$  for TCP decomposition with the change in the number of Fe–C bonds from 0–1 ns for (a)  $\alpha$ -Fe(110), (b)  $\text{Fe}_3\text{C}(010)$ , and (c)  $\text{Fe}_3\text{O}_4(001)$ .

end of the simulations, approximately five times as many P–O bonds were broken than C–O bonds, suggesting that P–O cleavage is the dominant decomposition mechanism. These observations are consistent with previous MD simulations<sup>39,44</sup> and experiments<sup>36</sup> of the thermal decomposition of TCP. Conversely, in previous NEMD simulations of trialkyl phosphates confined between  $\alpha$ -Fe(110) surfaces, the C–O bonds broke first and approximately twice as many C–O bonds were broken than P–O bonds.<sup>46</sup> The decomposition mechanism is therefore affected by the much stronger C–O bonds in triaryl phosphates compared to those in trialkyl phosphates. Moreover, unlike triaryl phosphates, some alkyl intermediates formed by C–O cleavage in trialkyl phosphates, such as butyl chains, can readily undergo  $\beta$ -hydride elimination reactions on ferrous surfaces to produce gaseous olefins.<sup>36</sup> In Fig. 8, the number of C–O and P–O bonds broken for the  $\alpha$ -Fe(110) and  $\text{Fe}_3\text{C}(010)$  surfaces is similar, but fewer bonds are broken for the  $\text{Fe}_3\text{O}_4(001)$  surfaces.

More P–O bonds are formed than are broken in the TCP molecules, leading to an overall increase in the number of P–O bonds, as shown by the solid red lines in Fig. 8. This is due to the formation of P–O–P linkages between the phosphorus atoms, resulting in polyphosphate chain growth.<sup>32,33</sup> This process occurs mainly through nucleophilic substitution reactions, whereby P–O–R bonds in TCP (where R is a cresyl group) are replaced by P–O–P bonds.<sup>46</sup>

The total increase in the number of P–O bonds at the end of the 1 ns simulation is similar (40–50 bonds) for the  $\alpha$ -Fe(110),

$\text{Fe}_3\text{C}(010)$ , and  $\text{Fe}_3\text{O}_4(001)$  surfaces. This is because both the P–O cleavage (blue dotted lines) and P–O formation (purple dotted lines) reactions are accelerated by the more reactive surfaces ( $\alpha$ -Fe(110)), as shown by the steeper lines in Fig. 8. The total number of P–O bonds at the end of the simulation is also not sensitive to the temperature and pressure, as shown in the ESI† (Fig. S4).<sup>46</sup>

For the  $\text{Fe}_3\text{O}_4(001)$  surface, nucleophilic attack from the surface oxygen atoms could increase the rate of P–O dissociation in the TCP molecules.<sup>44</sup> The variation in the number of P–O<sub>surf</sub> bonds formed between phosphorus atoms in the TCP molecules and oxygen atoms in the  $\text{Fe}_3\text{O}_4(001)$  surface is shown in the ESI† (Fig. S5). At low temperature and pressure, the number of P–O<sub>surf</sub> bonds formed (Fig. S4, ESI†) is much less than the total number of P–O bonds formed (Fig. 8), suggesting that this process plays a negligible role in the nucleophilic substitution reactions. However, at high temperature and pressure, the number of P–O<sub>surf</sub> bonds increases, such that it they represent a significant proportion (>10%) of the total P–O bonds formed. Overall, surface oxygen atoms do not seem to promote the decomposition of TCP on ferrous surfaces, as was suggested from previous experiments.<sup>32</sup>

### 3.5 Surface chemistry effects on polyphosphate growth

Fig. 9 shows the number of phosphate-containing oligomers, toluene, and cresol molecules formed from TCP at 500 K and 3 GPa on the three surfaces. On iron and iron carbide, the primary product of TCP decomposition is cresol, formed

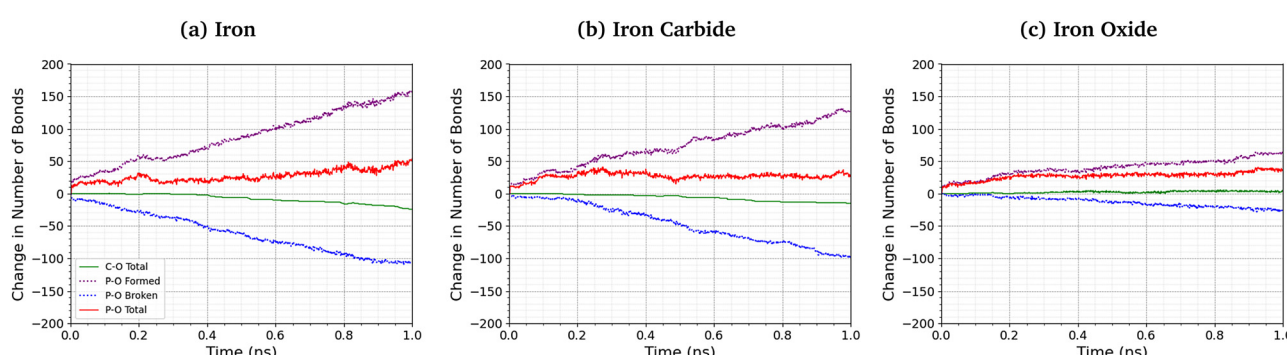


Fig. 8 Change in the number of P–O and C–O bonds with sliding time at 500 K and 3 GPa for the (a)  $\alpha$ -Fe(110), (b)  $\text{Fe}_3\text{C}(010)$ , and (c)  $\text{Fe}_3\text{O}_4(001)$  systems. Solid lines show the change in the total number of bonds compared to TCP, dashed lines show bond formation and dotted lines show bond cleavage.



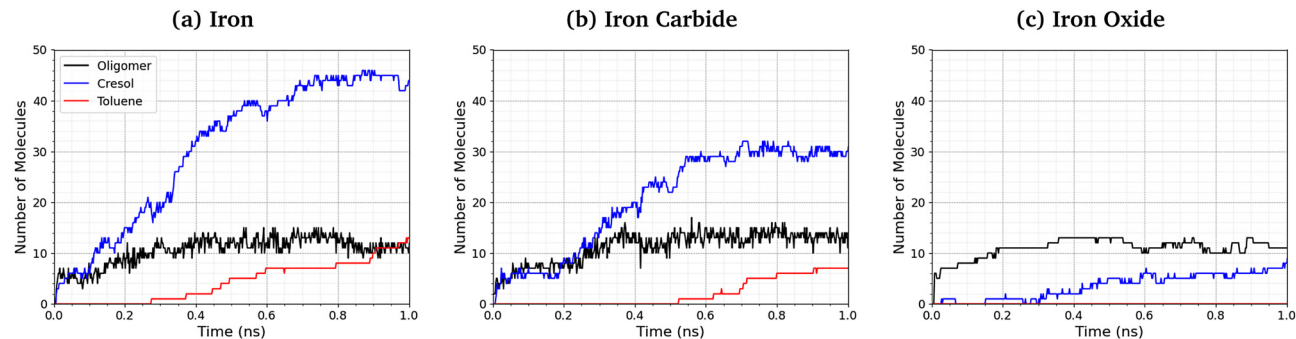


Fig. 9 Comparison of oligomer, toluene, and cresol quantities at 500 K and 3 GPa for the (a)  $\alpha$ -Fe(110), (b)  $\text{Fe}_3\text{C}(010)$ , and (c)  $\text{Fe}_3\text{O}_4(001)$  systems.

directly from P–O bond cleavage. Some toluene is also formed on these surfaces *via* C–O cleavage, but this occurs only after the formation of cresol. The number of oligomers formed is similar for all three surfaces. On iron oxide, phosphate-containing oligomers are the major product rather than cresol, due to the reduced rate of P–O cleavage reactions (Fig. 8).

The length of the polyphosphate chains in tribofilms is important to their antiwear performance.<sup>103</sup> Fig. 10 shows the change in the number of polyphosphate chains (dimers, trimers, tetramers, and  $\geq$  pentamers) with sliding time for the three studied systems. In all cases, the total number of polyphosphate fragments increases at short times before asymptoting towards a steady-state value of  $\sim 10$ . For  $\text{Fe}_3\text{C}(010)$  and  $\text{Fe}_3\text{O}_4(001)$ , the majority of TCP molecules form dimers, but longer chains, up to octomers, form in some cases. In general, longer polyphosphate chains are formed on the  $\alpha$ -Fe(110) surfaces than  $\text{Fe}_3\text{C}(010)$  and particularly  $\text{Fe}_3\text{O}_4(001)$  surfaces. For  $\alpha$ -Fe(110), a similar number of dimers and trimers form, with some of the chains growing up to octamers. The relatively short polyphosphate chains formed in our NEMD simulations are consistent with the average chain length of approximately 2.5 monomers found in tribometer experiments with ZDDP.<sup>103</sup> Much longer chains (up to 40 linked monomers) were formed in previous NEMD simulations with ReaxFF of phosphoric acid confined between sliding silica surfaces at very high temperature (1400 K).<sup>104</sup> The longer chains formed in these previous simulations is probably due to the higher reactivity of phosphoric acid compared to TCP and the lack of

iron atoms to catalyse the depolymerisation (P–O dissociation) reactions.

The difference in the polyphosphate chain length between the three surfaces is much more subtle than the change in TCP decomposition rates. This is probably because iron atoms or ions, which are most readily available in  $\alpha$ -Fe(110), accelerate the depolymerisation of the polyphosphate chains by P–O bond cleavage.<sup>103</sup> Similarly, the polyphosphate chain length does not vary significantly over the wide range of temperatures and pressures studied in the NEMD simulations, as shown in the ESI† (Fig. S6). This is because both the polymerisation (P–O formation) and depolymerisation (P–O dissociation) reactions are accelerated by a similar amount due to increased temperature and shear stress, as shown in the ESI† (Fig. S4).

### 3.6 Rate analysis

Fig. 11 shows the dependence of the TCP decomposition rate constant on shear stress for iron, iron carbide, and iron oxide surfaces. The Bell model<sup>95</sup> (eqn (1)) accurately describes the rate of TCP decomposition with temperature and shear stress on the three surfaces, as shown in the ESI† (Fig. S7). The activation volume,  $\Delta V^*$ , is calculated from the 2D fits of the rate *versus* shear stress data to eqn (1) shown in the insets of Fig. 11. With this 2D fitting method,  $\Delta V^*$  is found to increase monotonically with temperature from  $4.9 \pm 1.7 \text{ \AA}^3$  at 400 K to  $17.5 \pm 8.4 \text{ \AA}^3$  at 900 K for TCP between the  $\alpha$ -Fe(110) surfaces. In all cases, the activation volume is positive, which suggests that the rate determining step involves bond cleavage.<sup>96</sup> This

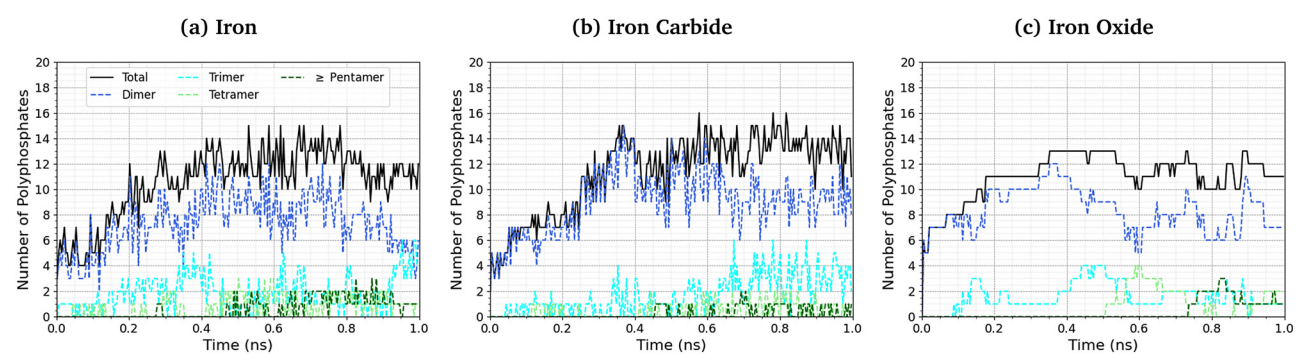


Fig. 10 Change in the number of polyphosphate chains with sliding time at 500 K and 3 GPa for (a)  $\alpha$ -Fe(110), (b)  $\text{Fe}_3\text{C}(010)$  and (c)  $\text{Fe}_3\text{O}_4(001)$  systems.

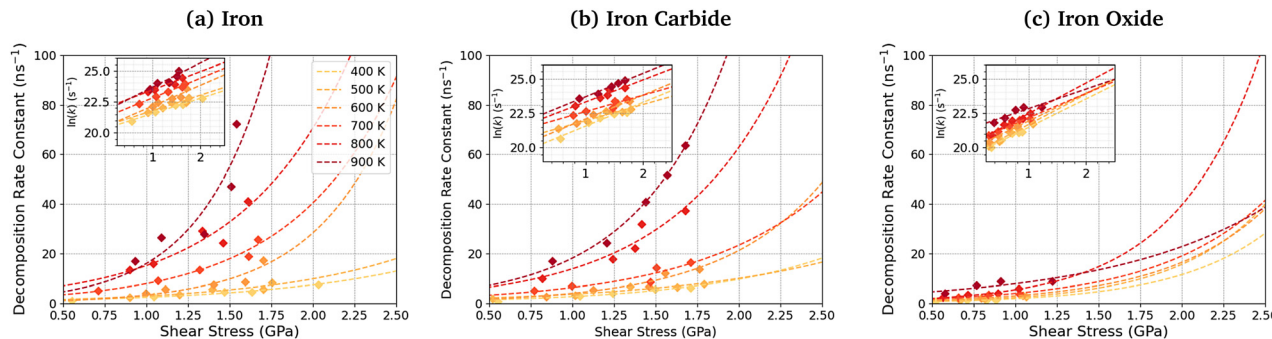


Fig. 11 Shear stress dependence of the TCP decomposition rate at different temperatures for (a)  $\alpha$ Fe(110), (b)  $\text{Fe}_3\text{C}(010)$ , and (c)  $\text{Fe}_3\text{O}_4(100)$  systems. Insets show the same data with a logarithmic y-axis.

observation is consistent with previous experiments of tribofilm growth from antiwear additives.<sup>91</sup> For the  $\text{Fe}_3\text{C}(010)$  surfaces,  $\Delta V^*$  also increases with temperature from  $6.6 \pm 3.7 \text{ \AA}^3$  at 400 K to  $15.3 \pm 2.4 \text{ \AA}^3$  at 900 K, while for the  $\text{Fe}_3\text{O}_4(100)$  surfaces,  $\Delta V^*$  increases from  $8.3 \pm 4.5 \text{ \AA}^3$  at 400 K to  $12.8 \pm 6.6 \text{ \AA}^3$  at 900 K. The calculated  $\Delta V^*$  values are all consistent with the dimensions of single bonds. The molecular volume of TCP is approximately  $500 \text{ \AA}^3$ , meaning that the activation volumes for TCP on the three surfaces range between 1 and 4% of the molecular volume. This percentage range is consistent with previous NEMD simulations using trialkyl phosphates (4%),<sup>46</sup> while experiments using ZDDPs with different alkyl substituent showed somewhat larger percentages (7–17%).<sup>54</sup>

Based on the 2D fits to eqn (1) shown in Fig. 11, the activation volume is highly temperature-dependant, but there are no clear differences between the three surfaces due to the relatively large uncertainties. Previous experimental studies of mechanochemical tribofilm growth have treated the activation volume as a temperature-independent reaction constant; however, these studies considered a much smaller temperature range than the present study.<sup>8–10,54,91</sup> In our recent NEMD study of trialkyl phosphate mechanochemical decomposition, we also observed that the activation volume increased with increasing temperature.<sup>46</sup> This was partially explained through a reduction in the elastic modulus of the  $\alpha$ -Fe(110) slabs.<sup>46</sup> A recent DFT study suggested that the contribution of the elastic deformation of the surrounding bulk to the activation volume of mechanochemical reactions can be significant and, in some cases, dominant.<sup>87</sup> The elastic modulus of all three surfaces decreases with increasing temperature (Table S1, ESI<sup>†</sup>). Since the activation volume is inversely proportional to the contact stiffness,<sup>87</sup> it is expected that higher temperatures will lead to lower activation energies, as observed in Fig. 11 and Table S4 (ESI<sup>†</sup>). However, the increase in the activation volume (up to 350%) is much larger than the decrease in the stiffness of the surfaces (up to 10%) between 400–900 K. Thus, other factors, such as a decrease in stiffness of the confined TCP molecules and its decomposition products, must also contribute to the increased activation volume at higher temperature.

The activation energy,  $E_a$ , is calculated from the slope of the 2D fits of eqn (1) to the rate *versus* inverse temperature data shown in the ESI<sup>†</sup> (Fig. S8). For TCP decomposition between

the  $\alpha$ -Fe(110) surfaces,  $E_a$  increases with pressure from  $20.6 \pm 5.5 \text{ kJ mol}^{-1}$  at 1 GPa to  $24.0 \pm 6.5 \text{ kJ mol}^{-1}$  at 5 GPa. For the  $\text{Fe}_3\text{C}(010)$  surfaces,  $E_a$  also increases from  $19.7 \pm 6.1 \text{ kJ mol}^{-1}$  at 1 GPa to  $24.3 \pm 7.5 \text{ kJ mol}^{-1}$  at 5 GPa. For the  $\text{Fe}_3\text{O}_4(100)$  surfaces,  $E_a$  again increases from  $10.2 \pm 7.2 \text{ kJ mol}^{-1}$  at 1 GPa to  $19.5 \pm 3.63 \text{ kJ mol}^{-1}$  at 5 GPa. A previous experimental study suggested that the thermal activation energy for TCP decomposition on stainless steel is approximately  $60 \text{ kJ mol}^{-1}$ .<sup>45</sup> Thus, the activation energy values are considerably underpredicted in our simulations compared to experiments,<sup>45</sup> which is probably due to the chromium-rich oxide layer formed on the surface of stainless steel in experiments.<sup>105</sup> Chromium oxide is known to be much less reactive towards TCP than iron oxide,<sup>33,34,57</sup> as was used in our NEMD simulations. Thus, the chromium oxide surface formed on stainless steel is expected to reduce the activation energy by a smaller amount than the iron oxides formed on conventional bearing steel.<sup>37,38</sup> From *in situ* tribometer experiments, the activation energy for TCP decomposition on an iron substrate was estimated as  $6.3 \text{ kJ mol}^{-1}$ ,<sup>106</sup> which is somewhat lower than our simulation results. This can be explained through the fact that the effect of shear stress on reducing the activation energy, as shown in eqn (1), was not considered in their calculations. As a result, the activation energy they calculated will be under-predicted.

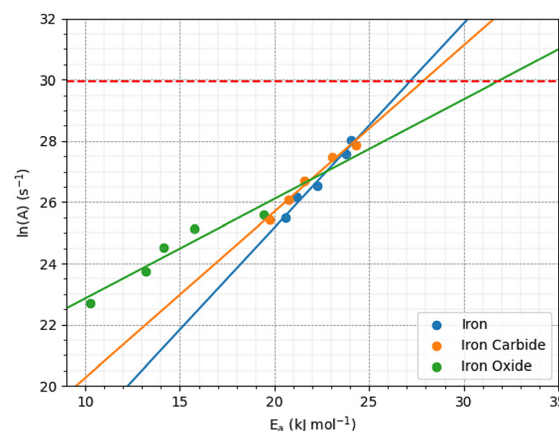


Fig. 12 Kinetic compensation effect between the activation energy and pre-exponential factor for iron, iron carbide, and iron oxide.



The pre-exponential factor,  $A$ , is calculated from the intercept of the fits of eqn (1) to the rate *versus* inverse temperature data shown in the ESI† (Fig. S8). This is often expressed as  $A = Z\rho$ , where  $Z$  is the frequency or collision factor, and  $\rho$  is the steric factor. The steric factor represents the fraction of successful collisions and is usually less than unity.<sup>107</sup> For TCP molecules between the  $\alpha$ -Fe(110) surfaces,  $\ln(A)$  increases with pressure from  $25.4 \pm 3.2$  at 1 GPa and to  $28.1 \pm 3.86$  at 5 GPa. For the  $\text{Fe}_3\text{C}(010)$  surfaces,  $\ln(A)$  increases from  $25.4 \pm 3.6$  at 1 GPa to  $27.8 \pm 4.7$  at 5 GPa, while it increases from  $22.6 \pm 4.5$  to  $25.6 \pm 2.1$  for the  $\text{Fe}_3\text{O}_4(100)$  surfaces. The low-pressure values are in very good agreement with previous estimates of the pre-exponential factor for the thermal decomposition of TCP on stainless steel at atmospheric pressure,  $\ln(A) = 22.7$ .<sup>45</sup>

Fig. 12 shows the variation of  $\ln(A)$  with  $E_a$  from the 2D fits to the rate *versus* temperature data. The concurrent increase in  $E_a$  with  $\ln(A)$ , which is known as the kinetic compensation effect, is often observed in heterogeneously catalysed processes.<sup>93</sup> Previous studies using ReaxFF to study the mechanochemical behaviours of trialkyl phosphates have also observed such an effect.<sup>46</sup> The presence of a compensation effect suggests that the changes in these parameters may have a mathematical rather than physical origin and does not necessarily indicate any changes to the reaction pathway.<sup>108</sup>

Experimental pre-exponential factors for surface reactions typically vary from  $10^{10}$ – $10^{16}$  s<sup>−1</sup>.<sup>109</sup> Some previous mechanochemistry studies<sup>8</sup> have used a constant pre-exponential factor of  $10^{13}$  s<sup>−1</sup> to determine the activation energy. If a constant pre-exponential factor of  $10^{13}$  s<sup>−1</sup> ( $\ln(A) = 30$ ) is used for all three surfaces (horizontal red dashed line in Fig. 12), the activation energies of TCP decomposition for the three surfaces from the 2D fits increase in the order  $\alpha\text{-Fe}(110) \sim \text{Fe}_3\text{C}(010) < \text{Fe}_3\text{O}_4(001)$ . Thus, the more reactive surfaces towards TCP give lower activation energies, which is consistent with previous experiments of  $\alpha$ -pinene tribopolymerisation.<sup>18</sup>

### 3.7 3D shear stress–temperature-rate constant fits

To investigate the combined influence of temperature and stress on reactivity, the decomposition rate data was also plotted as a 3D surface and fitted to eqn (1). This approach

provided significantly reduced uncertainties in the activation volume, activation energy, and pre-exponential factor compared to 2D fits in our previous NEMD study of trialkyl phosphate mechanochemistry.<sup>46</sup> The 3D fits for  $\alpha\text{-Fe}(110)$ ,  $\text{Fe}_3\text{C}(010)$  and  $\text{Fe}_3\text{O}_4(100)$  are presented in Fig. 13(a–c), respectively. To avoid biasing the 3D fits towards the higher decomposition rate constants, fits  $\ln(k)$ , rather than  $k$  were employed, as shown in the ESI† (Fig. S12).<sup>46</sup> Using the 3D surfaces, we calculated  $\Delta V^*$ ,  $E_a$ , and  $A$  values across the entire range of temperatures and pressures studied, as shown in Table 1. Unlike the 2D plots, the 3D fitting method does not capture the changes in the Bell model parameters with temperature and pressure. However, compared to the 2D fits, the 3D fits led to reduced uncertainties in all three parameters in eqn (1),<sup>46</sup> as shown in the ESI† (Fig. S7, S10 and S11).

The 3D fits suggest that the activation energy increases in the order:  $\text{Fe}_3\text{O}_4(100) < \text{Fe}_3\text{C}(010) \sim \alpha\text{-Fe}(110)$ , which is opposite to that expected from the relative reactivity of the surfaces. The smaller energy barrier for the less reactive oxide surfaces may be due to the availability of oxygen atoms to promote P–O dissociation through nucleophilic substitution reactions at the phosphorus atoms. On the other hand, the pre-exponential factor is also much smaller for the iron oxide surface, suggesting that the fraction of successful collisions is also much lower. This may be due to the decreased availability of iron atoms at the surface, which are essential to promoting the P–O dissociation reactions.

The  $\Delta V^*$  values increase in the order:  $\text{Fe}_3\text{O}_4(100) < \text{Fe}_3\text{C}(010) < \alpha\text{-Fe}(110)$ , suggesting that the more reactive surfaces lead to an increased shear stress dependence of the reactivity. The larger activation volume for  $\alpha\text{-Fe}(110)$  than  $\text{Fe}_3\text{C}(010)$  and particularly  $\text{Fe}_3\text{O}_4(100)$  could be because the more reactive surfaces anchor the TCP molecules, leading to more efficient transmission of shear stress applied through the surfaces to strain within the molecules. Similar suggestions have been made from previous NEMD simulations in other systems, which have shown accelerated mechanochemical reaction when molecules are anchored to one<sup>20</sup> or both<sup>21</sup> sliding surfaces. Our observation of higher  $\Delta V^*$  values on more reactive surfaces contrasts with previous experiments  $\alpha$ -pinene

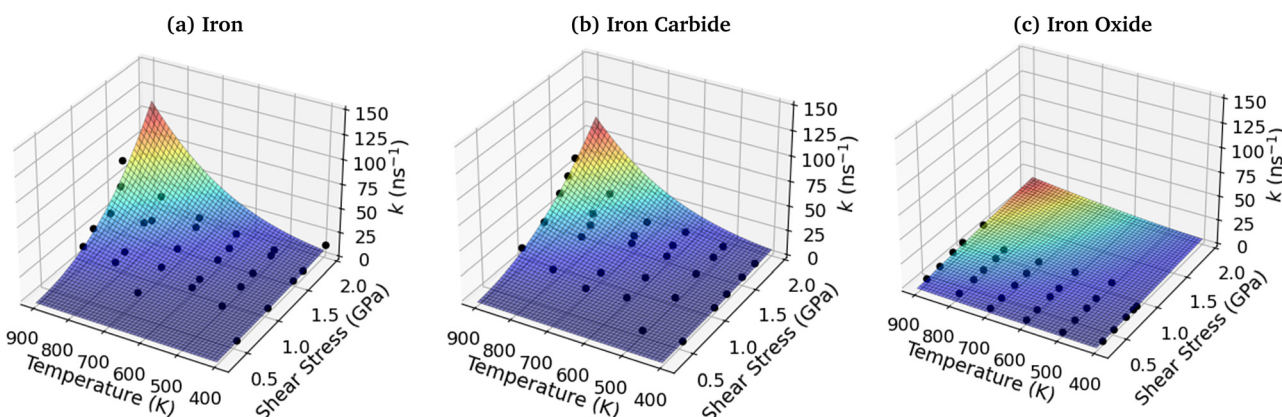


Fig. 13 3D fits of TCP decomposition rate as a function of temperature and shear stress for (a)  $\alpha$ -Fe(110), (b)  $\text{Fe}_3\text{C}(010)$  and (c)  $\text{Fe}_3\text{O}_4(100)$  surfaces.



**Table 1** Calculated values of the activation energy,  $E_a$ , natural logarithm of the pre-exponential factor,  $\ln(A)$ , and activation volume,  $\Delta V^*$ , for TCP between  $\alpha\text{-Fe}(110)$ ,  $\text{Fe}_3\text{C}(010)$  and  $\text{Fe}_3\text{O}_4(100)$  surfaces from the 3D fits to eqn (1). The parameter ranges represent the 95% confidence intervals from the 3D fits

Surface	$E_a$ (kJ mol <sup>-1</sup> )	$\ln(A)$ (s <sup>-1</sup> )	$\Delta V^*$ (Å <sup>3</sup> )
$\alpha\text{-Fe}(110)$	$21.3 \pm 2.8$	$27.0 \pm 2.0$	$12.3 \pm 3.3$
$\text{Fe}_3\text{C}(010)$	$22.1 \pm 2.6$	$26.2 \pm 1.7$	$10.2 \pm 2.6$
$\text{Fe}_3\text{O}_4(100)$	$11.2 \pm 1.7$	$24.3 \pm 1.8$	$8.1 \pm 4.4$

tribopolymerisation, which showed that surfaces that promoted  $\alpha$ -pinene chemisorption (e.g. copper oxide) gave smaller activation volumes than the ones only capable of physisorption (e.g. silicon oxide).<sup>18</sup> This discrepancy may be because the experiments studied bond-forming mechanochemical reactions, rather than bond-breaking as in the current simulations. The reaction yield was higher on the more reactive surfaces, implying that the accelerated reactivity for the more reactive surfaces seen in the experiments was mostly due to a reduction in activation energy (although this was not quantified).<sup>18</sup>

Another factor contributing to the difference in activation volumes between the three surfaces could be the contact stiffness.<sup>46,87</sup> In our NEMD simulations, at a given temperature, the stiffness of the three surfaces is quite similar (within 10%), as shown in the ESI† (Table S1). At most temperatures, the contact stiffness increases in the order  $\text{Fe}_3\text{C}(010) < \alpha\text{-Fe}(110) < \text{Fe}_3\text{O}_4(100)$ . Since the activation volume is expected to be inversely proportional to the contact stiffness,<sup>87</sup> the increased stiffness of the  $\text{Fe}_3\text{O}_4(100)$  surface may also contribute to its smaller activation volume compared to the other two surfaces. However, we expect that the differences in contact stiffness play a secondary role compared to the molecular adsorption strength in determining the variation in activation volume between the three surfaces.

## 4 Conclusions

We have studied the mechanochemical decomposition of TCP molecules confined between atomically-smooth iron, iron carbide, and iron oxide surfaces using NEMD simulations with ReaxFF. The iron surfaces are more effective in promoting TCP decomposition compared to iron carbide and particularly iron oxide surfaces, which correlates with the increase in Fe–C bonding between the molecules and the surface, as well as the surface energy. Once the molecules are adsorbed, decomposition of TCP proceeds through P–O bond dissociation for all of the surfaces to form cresol molecules. In some cases, a subsequent C–O bond dissociation within the cresol molecule leads to the formation of toluene.

The rate of TCP decomposition increases exponentially with temperature and shear stress, indicating that this is a SATA process. We show that the presence of DIDA base oil molecules does not affect the decomposition mechanism, but reduces the shear stress and thus the TCP decomposition rate. The change in the TCP decomposition rate constants with shear stress for

the systems with and without DIDA can be described with a single fit to the Bell model using the same activation volume. This observation justifies the use of base oil-free NEMD simulations for the subsequent wide parameter study.

As well as TCP decomposition, we also investigate the early stages of polyphosphate growth. Despite the fact that P–O bond formation is accelerated on the more reactive surfaces (iron), the rate of P–O bond cleavage is also increased by a similar amount, meaning that the total number of P–O bonds is comparable between the three surfaces. The polyphosphate chain length is also similar between the surfaces, with a skew in the distribution to higher chain lengths (up to octomers) for the more reactive iron surfaces.

3D fits to the Bell model lead to activation energies and pre-exponential factors both increasing in the order:  $\text{Fe}_3\text{O}_4(100) < \text{Fe}_3\text{C}(010) \sim \alpha\text{-Fe}(110)$ . This implies that, although the energy barrier is smaller for the less reactive oxide surfaces, the fraction of successful collisions is also much lower. This trend may be due to the decreased availability of iron atoms on the surface, which are essential to promoting the decomposition reactions. The activation energies and pre-exponential factors calculated from the NEMD simulations are within the experimental range reported for iron and stainless steel (chromium oxide) surfaces. The activation volume from the 3D fits increases in the order:  $\text{Fe}_3\text{O}_4(100) < \text{Fe}_3\text{C}(010) < \alpha\text{-Fe}(110)$ , which suggests that higher surface energy causes the TCP molecules to be anchored to the surface, leading to more efficient transmission of mechanical energy. An additional contribution to the larger activation energy for  $\alpha\text{-Fe}(110)$  surfaces could be the lower contact stiffness.

We have shown that surface chemistry plays a central role in the mechanochemical decomposition of an industrially-important additive for aviation lubricants. The differences between the three ferrous surfaces can be rationalised through parameters from the Bell model. Future NEMD simulations could consider the impact of heterogeneous, rough surfaces, such as steel on mechanochemical reactions. On the other hand, experiments could consider using more chemically controllable surfaces, such as specific iron oxides grown on top of atomically-smooth silicon wafers, for optimal comparison with molecular simulations of mechanochemistry within nanoscale contacts.

## Conflicts of interest

There are no conflicts to declare.

## Acknowledgements

E. O. thanks the Engineering and Physical Sciences Research Council (EPSRC) for PhD funding through their Doctoral Training Partnership (DTP) scheme (EP/T51780X/1). J. P. E. acknowledges the support of the Royal Academy of Engineering through their Research Fellowships scheme. J. P. E. and C. A. L. thank Shell and the EPSRC for funding *via* the InFUSE Prosperity



Partnership (EP/V038044/1). A. M. and F. H. B. acknowledge support from the National Science Foundation (NSF) grant CMMI-2038499. The authors acknowledge the use of Imperial College London Research Computing Service (<https://doi.org/10.14469/hpc/2232>) and the UK Materials and Molecular Modelling Hub, which is partially funded by the EPSRC (EP/T022213/1, EP/W032260/1 and EP/P020194/1). We thank Daniele Dini for useful discussions.

## References

- 1 R. T. O'Neill and R. Boulatov, *Nat. Rev. Chem.*, 2021, **5**, 148–167.
- 2 E. Colacino, M. Carta, G. Pia, A. Porcheddu, P. C. Ricci and F. Delogu, *ACS Omega*, 2018, **3**, 9196–9209.
- 3 S. L. James, C. J. Adams, C. Bolm, D. Braga, P. Collier, W. Jones, A. Krebs, J. Mack, L. Maini, A. G. Orpen, I. P. Parkin, W. C. Shearouse, W. Steed and D. C. Waddell, *Chem. Soc. Rev.*, 2012, **41**, 413–447.
- 4 A. A. Michalchuk, I. A. Tumanov and E. V. Boldyreva, *CrystEngComm*, 2019, **21**, 2174–2179.
- 5 R. A. Haley, A. R. Zellner, J. A. Krause, H. Guan and J. Mack, *ACS Sustainable Chem. Eng.*, 2016, **4**, 2464–2469.
- 6 S. Hwang, S. Gratz and L. Borchardt, *Chem. Commun.*, 2022, **58**, 1661–1671.
- 7 A. Boscoboinik, D. Olson, H. Adams, N. Hopper and W. T. Tysoe, *Chem. Commun.*, 2020, **56**, 7730–7733.
- 8 N. N. Gosvami, J. A. Bares, F. Mangolini, A. R. Konicek, D. G. Yablon and R. W. Carpick, *Science*, 2015, **348**, 102–106.
- 9 J. Zhang and H. Spikes, *Tribol. Lett.*, 2016, **63**, 24.
- 10 J. Zhang, J. P. Ewen, M. Ueda, J. S. Wong and H. A. Spikes, *ACS Appl. Mater. Interfaces*, 2020, **12**, 6662–6676.
- 11 A. Neville, A. Morina, T. Haque and M. Voong, *Tribol. Int.*, 2007, **40**, 1680–1695.
- 12 P. Mittal, Y. Maithani, J. P. Singh and N. N. Gosvami, *Tribol. Int.*, 2020, **151**, 106419.
- 13 C. McFadden, C. Soto and N. D. Spencer, *Tribol. Int.*, 1997, **30**, 881–888.
- 14 M. Ueda, A. Kadiric and H. Spikes, *Tribol. Online*, 2020, **15**, 318–331.
- 15 M. Ueda, A. Kadiric and H. Spikes, *Tribol. Lett.*, 2021, **69**, 62.
- 16 S. Peeters, A. Barlini, J. Jain, N. N. Gosvami and M. C. Righi, *Appl. Surf. Sci.*, 2022, **600**, 153947.
- 17 V. R. S. Ruiz, T. Kuwahara, J. Galipaud, K. Masenelli-Varlot, M. B. Hassine, C. Heau, M. Stoll, L. Mayrhofer, G. Moras, J. M. Martin, M. Moseler and M.-I. De Barros Bouchet, *Nat. Commun.*, 2021, **12**, 4550.
- 18 X. He and S. H. Kim, *Langmuir*, 2018, **34**, 2432–2440.
- 19 A. Khajeh, X. He, J. Yeon, S. H. Kim and A. Martini, *Langmuir*, 2018, **34**, 5971–5977.
- 20 J. Yeon, X. He, A. Martini and S. H. Kim, *ACS Appl. Mater. Interfaces*, 2017, **9**, 3142–3148.
- 21 T. Kuwahara, P. A. Romero, S. Makowski, V. Weihnacht, G. Moras and M. Moseler, *Nat. Commun.*, 2019, **10**, 151.
- 22 B. Guan, B. A. Pochopien and D. S. Wright, *Lubr. Sci.*, 2016, **28**, 257–265.
- 23 D. W. Johnson and J. E. Hils, *Lubricants*, 2013, **1**, 132–148.
- 24 O. Beeck, J. Givens and E. Williams, *Proc. R. Soc. London, Ser. A*, 1940, **177**, 103–118.
- 25 D. H. Han and M. Masuko, *Tribol. Trans.*, 1999, **42**, 902–906.
- 26 J. Airey, J. Simpson, M. Spencer, R. W. Greenwood and M. J. Simmons, *Proc. Inst. Mech. Eng., Part J*, 2023, **237**, 1548–1567.
- 27 R. L. Jones, H. Ravner and R. L. Cottingham, *ASLE Trans.*, 1970, **13**, 1–10.
- 28 F. Barcroft and S. Daniel, *J. Basic Eng.*, 1965, **87**, 761–767.
- 29 D. Godfrey, *ASLE Trans.*, 1965, **8**, 1–11.
- 30 O. D. Faut and D. R. Wheeler, *ASLE Trans.*, 1983, **26**, 344–350.
- 31 A. H. J. M. Gauthier, H. Montes and J. M. Georges, *ASLE Trans.*, 1982, **25**, 445–455.
- 32 C. Saba and N. Förster, *Tribol. Lett.*, 2002, **12**, 135–146.
- 33 D. W. Johnson, S. Morrow, N. H. Förster and C. S. Saba, *Chem. Mater.*, 2002, **14**, 3767–3775.
- 34 B. Acharya, T. Pardue, K. Avva and J. Krim, *Tribol. Int.*, 2018, **126**, 106–115.
- 35 D. R. Wheeler and O. D. Faut, *Appl. Surf. Sci.*, 1984, **18**, 106–122.
- 36 D. Sung and A. Gellman, *Tribol. Int.*, 2002, **35**, 579–590.
- 37 R. D. Evans, K. L. More, C. V. Darragh and H. P. Nixon, *Tribol. Trans.*, 2004, **47**, 430–439.
- 38 R. D. Evans, K. L. More, C. V. Darragh and H. P. Nixon, *Tribol. Trans.*, 2005, **48**, 299–307.
- 39 A. Khajeh, F. H. Bhuiyan, J.-E. Mogonye, R. A. Pesce-Rodriguez, S. Berkebile and A. Martini, *J. Phys. Chem. C*, 2021, **125**, 5076–5087.
- 40 H. K. D. H. Bhadeshia, *Prog. Mater. Sci.*, 2012, **57**, 268–435.
- 41 D. W. Johnson, J. E. Hils and N. Förster, *Tribol. Lett.*, 2011, **42**, 223–232.
- 42 A. Stukowski, *Modell. Simul. Mater. Sci. Eng.*, 2009, **18**, 015012.
- 43 A. Khajeh, X. Hu, K. Mohammadtabar, Y. K. Shin, A. C. Van Duin, S. Berkebile and A. Martini, *J. Phys. Chem. C*, 2019, **123**, 12886–12893.
- 44 J. P. Ewen, C. A. Latorre, C. Gattinoni, A. Khajeh, J. D. Moore, J. E. Remias, A. Martini and D. Dini, *J. Phys. Chem. C*, 2020, **124**, 9852–9865.
- 45 J. F. Makki and E. E. Graham, *Tribol. Trans.*, 1990, **33**, 595–603.
- 46 C. Ayestarán Latorre, J. E. Remias, J. D. Moore, H. A. Spikes, D. Dini and J. P. Ewen, *Commun. Chem.*, 2021, **4**, 178.
- 47 J. P. Ewen, D. M. Heyes and D. Dini, *Friction*, 2018, **6**, 349–386.
- 48 C. Winder and J. C. Balouet, *Environ. Res.*, 2002, **89**, 146–164.
- 49 R. Lu, K. Kobayashi, H. Nanao and S. Mori, *Tribol. Lett.*, 2009, **33**, 1–8.
- 50 E. E. Klaus, J. Phillips, S. C. Lin, N. L. Wu and J. L. Duda, *Tribol. Trans.*, 1990, **33**, 25–32.



51 P. Blonski and A. Kiejna, *Surf. Sci.*, 2007, **601**, 123–133.

52 W. C. Chiou and E. A. Carter, *Surf. Sci.*, 2003, **530**, 88–100.

53 R. Bliem, E. McDermott, P. Ferstl, M. Setvin, O. Gamba, J. Pavelec, M. A. Schneider, M. Schmid, U. Diebold, P. Blaha, L. Hammer and G. S. Parkinson, *Science*, 2014, **346**, 1215–1218.

54 J. Zhang, J. P. Ewen and H. A. Spikes, *Mol. Syst. Des. Eng.*, 2022, **7**, 1045–1055.

55 G. L. Clark and J. V. Robinson, *J. Am. Chem. Soc.*, 1940, **62**, 1948–1951.

56 S. Ramachandran, B. L. Tsai, M. Blanco, H. Chen, Y. Tang and W. A. Goddard, *Langmuir*, 1996, **12**, 6419–6428.

57 M. Abdelmaksoud, J. W. Bender and J. Krim, *Tribol. Lett.*, 2002, **13**, 179–186.

58 E. E. Graham and E. E. Klaus, *ASLE Trans.*, 1986, **29**, 229–234.

59 K. Mohammadtabar, S. J. Eder, N. Dörr and A. Martini, *Tribol. Int.*, 2022, **176**, 107922.

60 S. Hayashi, N. Uemura, M. Uranagase and S. Ogata, *J. Comput. Chem.*, 2023, **44**, 766–776.

61 S. Loehlé and M. Righi, *Lubricants*, 2018, **6**, 31.

62 K. Mohammadtabar, S. J. Eder, N. Dörr and A. Martini, *J. Phys. Chem. C*, 2019, **123**, 19688–19692.

63 S. Peeters, C. Charrin, I. Duron, S. Loehlé, B. Thiebaut and M. C. Righi, *Mater. Today Chem.*, 2021, **21**, 100487.

64 L. Wang and R. J. Wood, *Tribol. Int.*, 2007, **40**, 1655–1666.

65 D. W. Johnson, M. Bachus and J. E. Hils, *Lubricants*, 2013, **1**, 48–60.

66 A. P. Thompson, H. M. Aktulga, R. Berger, D. S. Bolintineanu, W. M. Brown, P. S. Crozier, P. J. in't Veld, A. Kohlmeyer, S. G. Moore and T. D. Nguyen, *et al.*, *Comput. Phys. Commun.*, 2022, **271**, 108171.

67 L. Verlet, *Phys. Rev.*, 1967, **159**, 98.

68 T. Schneider and E. Stoll, *Phys. Rev. B: Solid State*, 1978, **17**, 1302–1322.

69 X. Yong and L. T. Zhang, *J. Chem. Phys.*, 2013, **138**, 084503.

70 F. H. Bhuiyan, S. H. Kim and A. Martini, *Appl. Surf. Sci.*, 2022, **591**, 153209.

71 M. Koyama, J. Hayakawa, T. Onodera, K. Ito, H. Tsuboi, A. Endou, M. Kubo, C. A. D. Carpio and A. Miyamoto, *J. Phys. Chem. B*, 2006, **110**, 17507–17511.

72 S. J. Plimpton and A. P. Thompson, *MRS Bull.*, 2012, **37**, 513–521.

73 A. C. Van Duin, S. Dasgupta, F. Lorant and W. A. Goddard, *J. Phys. Chem. A*, 2001, **105**, 9396–9409.

74 T. P. Senftle, S. Hong, M. M. Islam, S. B. Kylasa, Y. Zheng, Y. K. Shin, C. Junkermeier, R. Engel-Herbert, M. J. Janik and H. M. Aktulga, *et al.*, *npj Comput. Mater.*, 2016, **2**, 1–14.

75 A. Martini, S. J. Eder and N. Dörr, *Lubricants*, 2020, **8**, 44.

76 M. Aryanpour, A. C. van Duin and J. D. Kubicki, *J. Phys. Chem. A*, 2010, **114**, 6298–6307.

77 C. Zou, A. C. Van Duin and D. C. Sorescu, *Top. Catal.*, 2012, **55**, 391–401.

78 C. Verlackt, E. Neyts, T. Jacob, D. Fantauzzi, M. Golkaram, Y. K. Shin, A. Van Duin and A. Bogaerts, *New J. Phys.*, 2015, **17**, 103005.

79 K. Chenoweth, A. C. V. Duin and W. A. Goddard, *J. Phys. Chem. A*, 2008, **112**, 1040–1053.

80 A. K. Rappe and W. A. Goddard III, *J. Phys. Chem.*, 1991, **95**, 3358–3363.

81 L. S. Morrissey, S. M. Handrigan, S. Subedi and S. Nakhla, *Mol. Simul.*, 2019, **45**, 501–508.

82 J. J. Adams, D. Agosta, R. Leisure and H. Ledbetter, *J. Appl. Phys.*, 2006, **100**, 113530.

83 J. Li, H. K. Mao, Y. Fei, E. Gregoryanz, M. Eremets and C. S. Zha, *Phys. Chem. Miner.*, 2002, **29**, 166–169.

84 H. J. Reichmann and S. D. Jacobsen, *Am. Mineral.*, 2004, **89**, 1061–1066.

85 M. M. Islam, C. Zou, A. C. V. Duin and S. Raman, *Phys. Chem. Chem. Phys.*, 2015, **18**, 761–771.

86 T. D. Ta, H. M. Le, A. K. Tieu, H. Zhu, H. T. T. Ta, N. V. Tran, S. Wan and A. C. T. van Duin, *ACS Appl. Nano Mater.*, 2020, **3**, 2687–2704.

87 Z. Li and I. Szlufarska, *Phys. Rev. Lett.*, 2021, **126**, 076001.

88 G. Clavier, N. Desbiens, E. Bourasseau, V. Lachet, N. Brusselle-Dupend and B. Rousseau, *Mol. Simul.*, 2017, **43**, 1413–1422.

89 K. Sebeck, C. Shao and J. Kieffer, *ACS Appl. Mater. Interfaces*, 2016, **8**, 16885–16896.

90 J. Zhang, A. Tan and H. Spikes, *Tribol. Lett.*, 2017, **65**, 13.

91 L. Fang, S. Korres, W. A. Lamberti, M. N. Webster and R. W. Carpick, *Faraday Discuss.*, 2023, **241**, 394–412.

92 X. Chen, K. Kawai, H. Zhang, K. Fukuzawa, N. Koga, S. Itoh and N. Azuma, *J. Phys. Chem. C*, 2020, **124**, 22496–22505.

93 E. Roduner, *Chem. Soc. Rev.*, 2014, **43**, 8226–8239.

94 H. Spikes, *Friction*, 2018, **6**, 1–31.

95 G. I. Bell, *Science*, 1978, **200**, 618–627.

96 B. Chen, R. Hoffmann and R. Cammi, *Angew. Chem., Int. Ed.*, 2017, **56**, 11126–11142.

97 J. P. Gao, W. D. Luedtke, D. Gourdon, M. Ruths, J. N. Israelachvili and U. Landman, *J. Phys. Chem. B*, 2004, **108**, 3410–3425.

98 X. Yu, C. F. Huo, Y. W. Li, J. Wang and H. Jiao, *Surf. Sci.*, 2012, **606**, 872–879.

99 S. J. Eder, A. Vernes and G. Betz, *Langmuir*, 2013, **29**, 13760–13772.

100 S. S. Tafreshi, A. Roldan, N. Y. Dzade and N. H. De Leeuw, *Surf. Sci.*, 2014, **622**, 1–8.

101 E. Osei-Agyemang, S. Berkebile and A. Martini, *Tribol. Lett.*, 2018, **66**, 1–22.

102 N. Y. Dzade, A. Roldan and N. H. de Leeuw, *Minerals*, 2014, **4**, 89–115.

103 R. Heuberger, A. Rossi and N. D. Spencer, *Tribol. Lett.*, 2007, **25**, 185–196.

104 D. C. Yue, T. B. Ma, Y. Z. Hu, J. Yeon, A. C. V. Duin, H. Wang and J. Luo, *J. Phys. Chem. C*, 2013, **117**, 25604–25614.

105 C. A. Olsson and D. Landolt, *Electrochim. Acta*, 2003, **48**, 1093–1104.

106 K. Sasaki, N. Inayoshi and K. Tashiro, *Wear*, 2010, **268**, 911–916.

107 M. G. Evans and M. Polanyi, *Trans. Faraday Soc.*, 1935, **31**, 875–894.

108 P. J. Barrie, *Phys. Chem. Chem. Phys.*, 2012, **14**, 318–326.

109 H. Lynggaard, A. Andreasen, C. Stegelmann and P. Stoltze, *Prog. Surf. Sci.*, 2004, **77**, 71–137.

